Progress In Electromagnetics Research M, Vol. 116, 103–118, 2023

Structure of the Field behind a Dielectric Circular Cylinder in the Lit Side of the Transition Region

Xin Du* and Jun-Ichi Takada

Abstract—Prediction in the transition region between lit and shadowed regions is important for maintaining stable mobile communication for the beyond 5^{th} generation. In this paper, as the difference between the reflection and diffraction from a dielectric circular cylinder and an absorber screen, respectively, a novel additional term is derived from a uniform theory of diffraction (UTD) in the lit side of the transition region. The proposed model is validated by the UTD and exact solutions of a dielectric circular cylinder. Through the proposal, we can separate the contribution of the shadowed Fresnel zone (FZ) number and boundary conditions (i.e., the surface impedance and the polarization) to the total field. The frequency characteristics of the shadowed FZ and boundary conditions are theoretically analyzed. The analyzed results show that the contributions of the boundary conditions are weaker than the shadowed FZ in the lit region at a high frequency.

1. INTRODUCTION

In order to meet the data traffic demands for the beyond 5^{th} generation (B5G) mobile communication systems, millimeter-wave (mmWave) and terahertz (THz) band radios are considered to use [1–3]. At these bands, since the human blockage significantly influences the line-of-sight (LoS) cellphone link performance, the use of a massive multiple-input and multiple-output (MIMO) to create other propagation paths is needed [4, 5]. For stable mobile communication, the prediction before the shadowing event occurred (i.e., the prediction in the lit side of the transition region) is important to evaluate the timing of the path shifting [6]. Therefore, fast prediction techniques in the lit side of the transition region are necessary. For a lower computational cost, the Kirchhoff approximation (KA) [7–9] and the uniform theory of diffraction (UTD) [10–14] have been widely used. Although the KA can achieve a good balance between accuracy and computational cost, the computational cost increases when the frequency becomes higher. On the other hand, the UTD has closed-form analytic solutions, resulting in a lower computational cost.

There are mainly two types of UTD models for the forward scattering problems of the human body. One of them models the human body as an absorber screen and calculates the edge diffraction [15–17]. The other considers the human body as a dielectric circular cylinder and evaluates the scattered field as the reflected and creeping diffracted fields in the lit and shadowed regions, respectively [18–21]. In the shadowed region, the cylinder model is in fact rather commonly used since the screen model lacks the creeping waves, which play an important role [12]. However, in the lit region, the measurement results in [4] reported that the screen model predicted the received power level with a negligible discrepancy. It is implied that in the lit region, an absorber screen may have similar accuracy to a dielectric circular cylinder model.

Received 23 February 2023, Accepted 6 April 2023, Scheduled 12 April 2023
* Corresponding author: Xin Du (du.x.ab@m.titech.ac.jp).
The authors are with the Department of Transdisciplinary Science and Engineering, School of Environment and Society, Tokyo Institute of Technology, Japan.

The diffraction from an absorber screen is determined by the shadowed Fresnel zone number (FZ) alone, which is explained in Appendix A. On the other hand, the reflection from a dielectric circular cylinder is determined by not only the shadowed FZ but also the boundary conditions (i.e., surface impedance and polarization). The previous work in [22] investigated different models to represent the human body, including the circular cylinders with different dielectric properties and the knife-edge model. The simulation and measurement results in [22] show that there is no significant discrepancy among those models in the lit region. It means that the contributions of the boundary conditions are weaker than the shadowed FZ in the lit region. However, the previous work in [22] did not provide a theoretical analysis to discuss the above results. If the difference between the reflection from a dielectric circular cylinder and diffraction from an absorber screen can be derived, the roles of the FZ and boundary conditions will be deeply clarified. However, the current UTD works [10–14] have not yet discussed the relationship between diffraction and reflection.

This paper aims to derive an additional term between the reflection from a dielectric circular cylinder and the diffraction from an absorber screen in the lit side of the transition region. From the proposal, the roles of the FZ and boundary condition are discussed by using a theoretical analysis of the frequency characteristics. The remainder of this paper is organized as follows. The proposed model is described in Section 2. The validation of the proposal by using the UTD and exact solutions of a dielectric circular cylinder is conducted, and the results are shown in Section 3. As the application of the proposed model, the frequency characteristics of the FZ and boundary condition are theoretically analyzed, and their roles are explained in Section 4. Finally, a conclusion as well as the limitation of this work and future work are given in Section 5.

2. PROPOSED MODEL

This section proposes an additional term between the reflection from a dielectric circular cylinder and the diffraction from an absorber screen with the same shadowed FZ. For the sake of simplicity, the two-dimensional (2D) problems of the infinite-height objects with an incident plane wave are considered. As shown in Fig. 1, the diffracted field from an absorber screen derived from [10, 11] can be calculated as

$$E^d = E^i D \frac{e^{-jk_0 s^d}}{\sqrt{s^d}} \tag{1}$$

$$D = \frac{-e^{-j\frac{\pi}{4}}}{4\sqrt{2\pi k_0}} \cot\frac{\pi - (\phi^d - \phi^i)}{4} F\left(k_0 s^d g^-(\phi^d - \phi^i)\right) \tag{2}$$

where E^i is the incident field to the object. D is the diffraction coefficient of an absorber screen. E^d is the diffracted field from the object. k_0 is the wave number in the free space. s^d is the distance from the diffraction point to the receiver (Rx). ϕ^i and ϕ^d are the angles of the incident and diffracted rays, respectively, measured in a plane perpendicular to the edge at the diffraction point. $F(\cdot)$ and $g^-(\cdot)$ are the modified Fresnel integral and a measure of the angular separation, respectively, mentioned in [10].

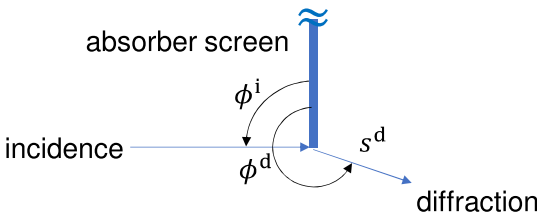

Figure 1. Diffraction from an absorber screen (top view).

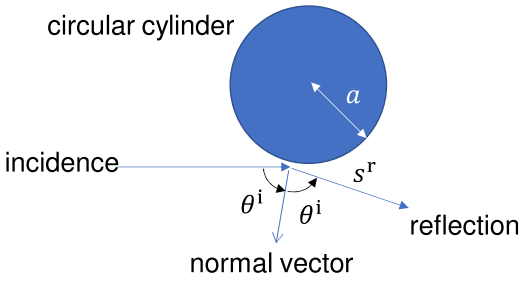

Figure 2. Reflection from a dielectric circular cylinder (top view).

On the other hand, the reflected field from a dielectric circular cylinder as shown in Fig. 2 is explained in [12–14] and is calculated as

$$E^r_{s,h} = E^i R_{s,h} \sqrt{\frac{a\cos\theta^i}{a\cos\theta^i + 2s^r}}\, e^{-jk_0 s^r} \tag{3}$$

$$R_{s,h} = -\sqrt{\frac{-4}{\xi}}\, e^{-j\frac{\xi^3}{12}} \left\{ \frac{e^{-j\frac{\pi}{4}}}{2\sqrt{\pi}\xi}[1 - F(X)] + \hat{P}(\xi, q_{s,h}) \right\} \tag{4}$$

$$\xi = -2M\cos\theta^i \tag{5}$$

$$X = \frac{k_0 s^r \xi^2}{2M^2} \tag{6}$$

$$q_{s,h} = -jM \left(\frac{\eta_0}{\eta_d}\right)^{\pm 1} \tag{7}$$

$$M = \left(\frac{k_0 a}{2}\right)^{\frac{1}{3}} \tag{8}$$

where R_s and R_h are the reflection coefficients for the perpendicular polarization (soft) and parallel polarization (hard), respectively. $E^r_{s,h}$ is the reflected field. a is the radius of the circular cylinder. s^r is the distance from the reflection point to the Rx. θ^i is the incident angle. M, ξ, X, and $q_{s,h}$ are the UTD parameters mentioned in [12–14]. The $\pm$ sign in (7) is directly associated with the s, h subscript of R. η_0 and η_d denote the free-space impedance and surface impedance of the dielectric cylinder, respectively. $\hat{P}(\cdot)$ is the Fock-type integral discussed in [14].

Using (1) and (3), the authors propose an additional term $A_{s,h}$ between the reflected and diffracted fields as

$$E^r_{s,h} \approx E^d + A_{s,h} \tag{9}$$

$$A_{s,h} := -E^i M \sqrt{\frac{2}{k_0}}\, p^*(\xi, q_{s,h}) e^{-j\frac{\xi^3}{12}}\, e^{-j\frac{\pi}{4}} \frac{e^{-jk_0 s}}{\sqrt{s}} \tag{10}$$

where $p^*(\cdot)$ is the associated Fock-type integral. s denotes either s^d or s^r. The detailed derivations are shown in Appendix B.

From (B2) in Appendix B, we should emphasize the angle ϕ^i should always be 90 degrees to maintain the assumption of the supplementary angle of $2\theta^i$. Thus, the diffraction E^d in (9) should be generated by the screen perpendicular to the direction of the incidence. However, that does not lose the generality of the proposed formula in the lit side. In case of an oblique incidence, the proposal still works, as shown in Fig. 3.

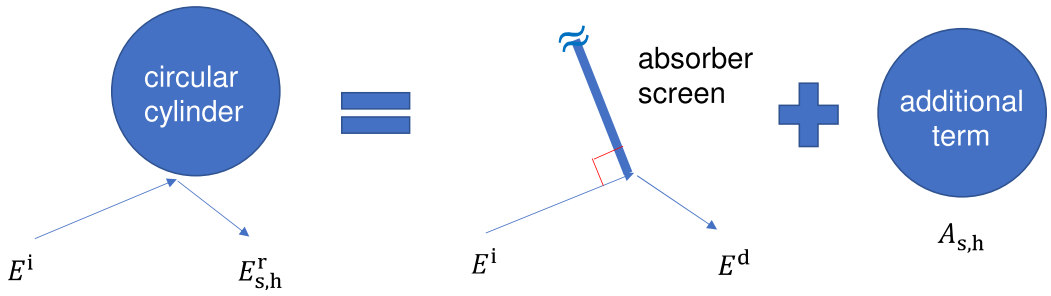

Figure 3. Model of the proposal in case of an oblique incidence.

3. VALIDATION OF PROPOSAL

In this section, the simulations using the UTD and the exact solution of a dielectric circular cylinder are conducted for validating the proposed model. Specifically, the validation is designed to evaluate

the effect of the additional term $A_{s,h}$ in (9). Therefore, the diffracted field E^d is compared with the reflected field $E^r_{s,h}$ with and without the additional term $A_{s,h}$.

As shown in Figs. 4(a)–4(b), the simulation environments use a semi-infinite-long screen and a dielectric circular cylinder to evaluate the diffraction and reflection, respectively. A uniform plane wave is normally incident upon the object. The parameters x and d are distances perpendicular and parallel to the incidence from the object to the Rx, respectively. The frequency f is considered at the mmWave and THz bands. By considering the human-shadowing problem, the relative complex permittivity ϵ_r of the human skin [23] is used, and the radius a of the circular cylinder is set as shown in Table 1. The real and imaginary parts of ϵ_r correspond to the relative permittivity and conductivity, respectively.

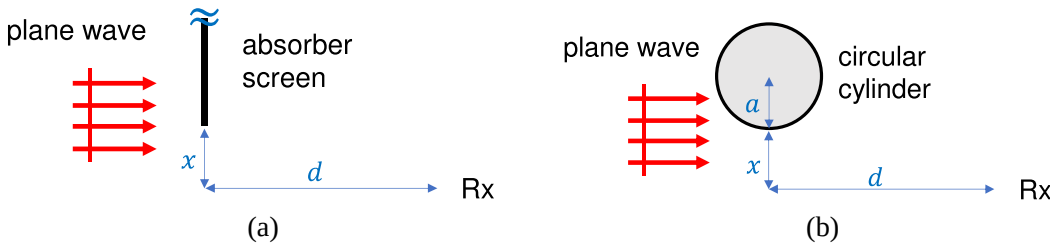

Figure 4. Simulation environment. (a) Environment of an absorber screen. (b) Environment of a dielectric circular cylinder.

Table 1. Simulation parameters.

Parameters	Values
f (GHz)	$40, 60, 80, 100$
x (m)	$[0, 0.3]$
d (m)	2
a (m)	0.25
ϵ_r	$11.7 - j14.3$ (at 40 GHz) $8.0 - j10.9$ (at 60 GHz) $6.4 - j8.6$ (at 80 GHz) $5.6 - j7.1$ (at 100 GHz)
E^i (V/m)	1

Four methods are simulated, i.e., the UTD (circular cylinder), UTD (screen), proposal, and exact solution. As a reference of accuracy, the exact solution is used and calculates the total field by using the eigen-function expansions as shown in Appendix C. In the UTD (circular cylinder), the total field is calculated as the sum of the reflected and creeping diffracted fields from a circular cylinder and an incident field. Compared with the UTD (circular cylinder), the UTD (screen) replaces the reflected field $E^r_{s,h}$ with the diffracted field E^d from a screen. The proposal introduces the additional term $A_{s,h}$ into the UTD (screen).

The processor of the calculating computer is an Intel(R) Core(TM) i9-12900K CPU @ 3.19 GHz. The usable installed memory of the calculating computer is 63.7 GB. The system type of the calculating computer is a 64-bit operating system with an x64-based processor. The simulation software is MATLAB.

Figures 5–8 show the plots of the spatial distributions of the normalized receiving power (NRP), which is the power density of the total field normalized by an incident field, at 40, 60, 80, and 100 GHz, respectively. For each frequency band, both perpendicular polarization (soft) and parallel polarization (hard) are simulated. x is varied from 0 to 0.3 m with an interval of 0.015 m, and hence each figure has 200 tests. The results show that the proposal is a good agreement with the exact solution. Considering

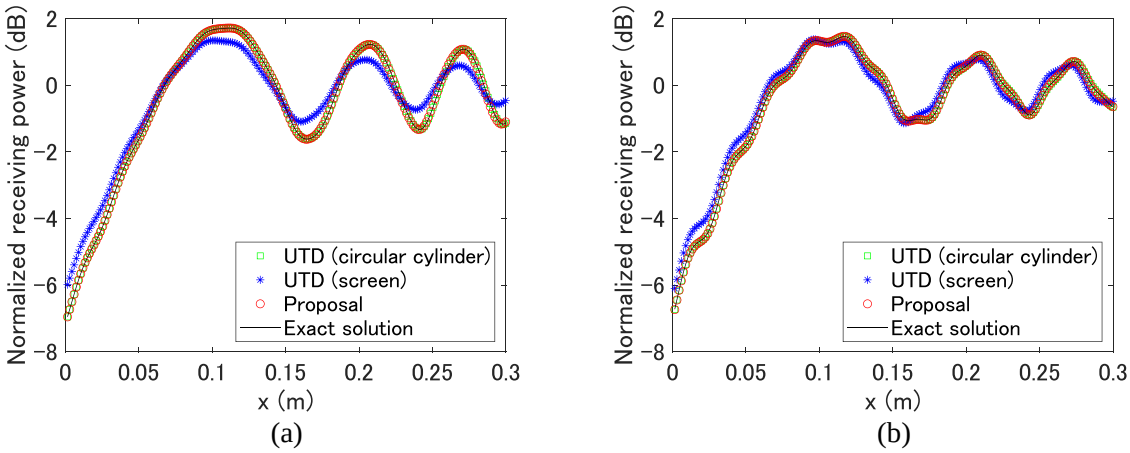

Figure 5. Validation of the proposed model at 40 GHz band. (a) Perpendicular polarization. (b) Parallel polarization.

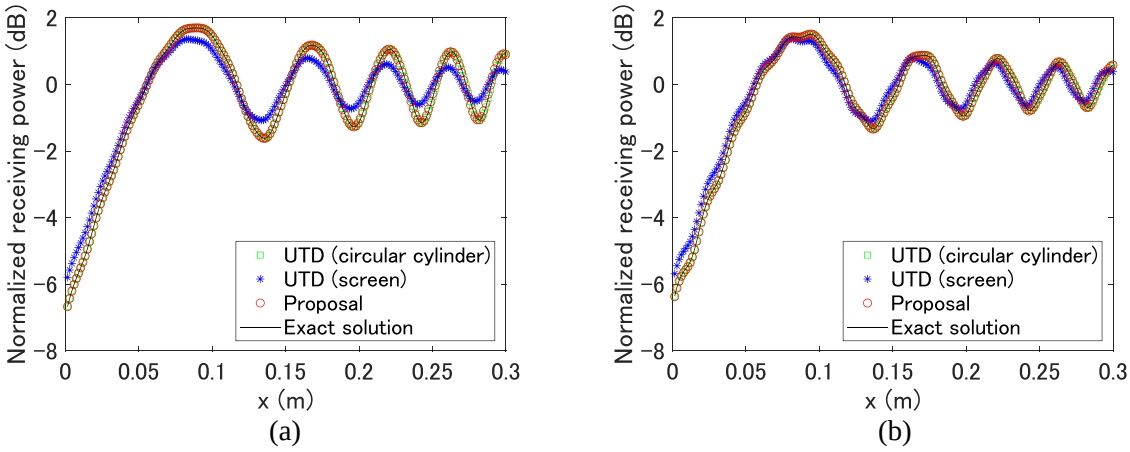

Figure 6. Validation of the proposed model at 60 GHz band. (a) Perpendicular polarization. (b) Parallel polarization.

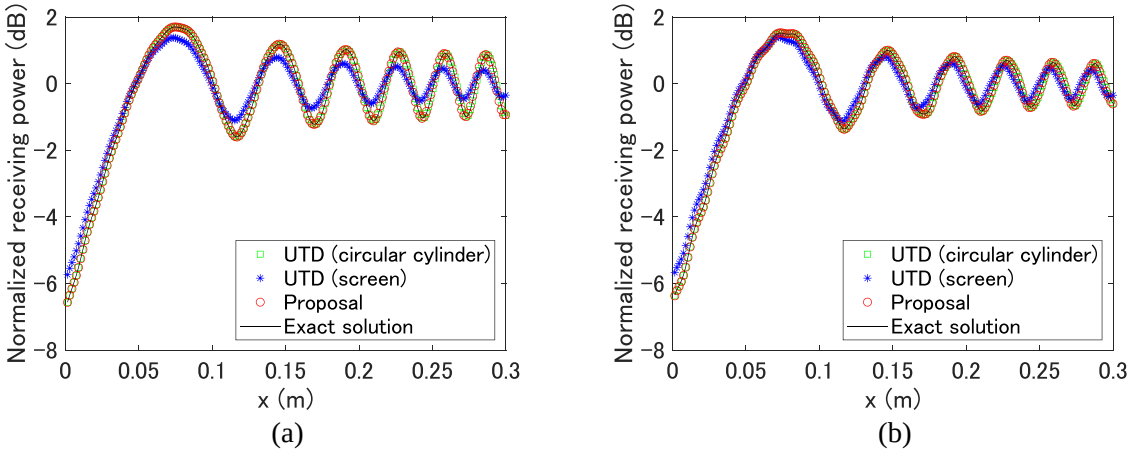

Figure 7. Validation of the proposed model at 80 GHz band. (a) Perpendicular polarization. (b) Parallel polarization.

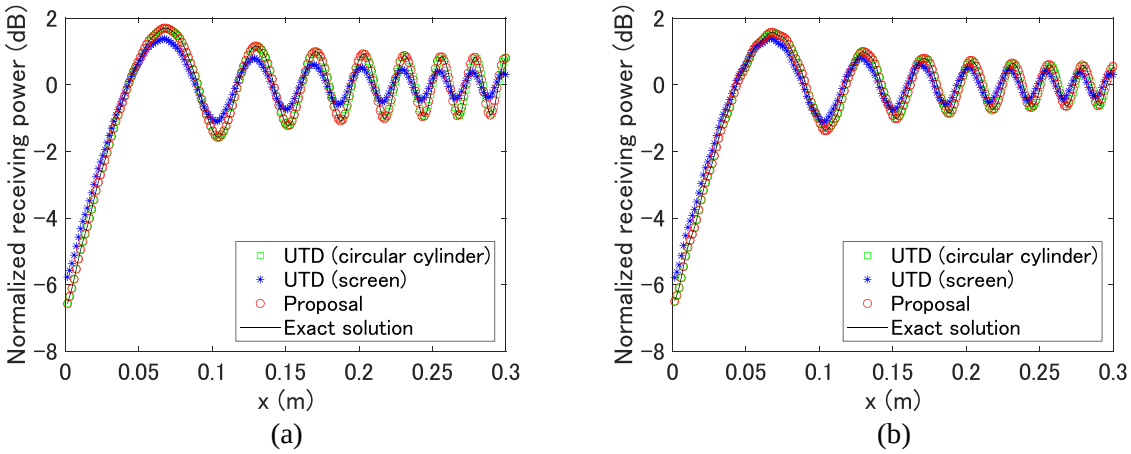

Figure 8. Validation of the proposed model at 100 GHz band. (a) Perpendicular polarization. (b) Parallel polarization.

the exact solution as a reference, the authors calculate the root-mean-square error (RMSE) by (11).

$$\mathrm{RMSE} = \sqrt{\sum_{i=1}^{m} \frac{\left(\mathrm{NRP}_i^{\mathrm{Method}} - \mathrm{NRP}_i^{\mathrm{Exact}}\right)^2}{m}} \tag{11}$$

where $\mathrm{NRP}_i^{\mathrm{Exact}}$ is the NRP calculated by the exact solution on a dB scale for the i^{th} test. $\mathrm{NRP}_i^{\mathrm{Method}}$ is the NRP calculated by the other methods on a dB scale for the i^{th} test. m is the total number of tests per figure (i.e., $m = 200$). The comparison of the RMSE among all the methods is shown in Table 2.

Table 2. The comparison of the RMSE among the UTD (circular cylinder), UTD (screen), and proposal.

Methods	UTD (circular cylinder)	UTD (screen)	This work
40 GHz (soft)	0.00 dB	0.43 dB	0.03 dB
40 GHz (hard)	0.01 dB	0.29 dB	0.02 dB
60 GHz (soft)	0.00 dB	0.40 dB	0.04 dB
60 GHz (hard)	0.01 dB	0.30 dB	0.03 dB
80 GHz (soft)	0.00 dB	0.39 dB	0.05 dB
80 GHz (hard)	0.01 dB	0.30 dB	0.03 dB
100 GHz (soft)	0.00 dB	0.37 dB	0.06 dB
100 GHz (hard)	0.01 dB	0.30 dB	0.04 dB

The results show that the UTD (screen) has an accuracy with an RMSE of over 0.1 dB. However, the proposed model achieves a good accuracy with a low RMSE of less than 0.1 dB as well as the UTD (circular cylinder), compared with the exact solution. Therefore, the proposal is validated.

4. APPLICATION OF PROPOSAL

Although the proposed model can only provide the same accuracy as the traditional UTD (circular cylinder), the proposal can be applicable to theoretically analyze the contribution of the shadowed FZ and boundary conditions. Since the diffracted field E^d is only determined by the shadowed FZ alone while the key factor $q_{s,h}$ corresponding to the boundary conditions (i.e., surface impedance and the

polarization) is only included in the additional term $A_{s,h}$, the contribution of the shadowed FZ and boundary conditions can be separated by (9).

To evaluate the contribution of each term to the total field, where a weak creeping diffraction is neglected, the frequency characteristics of the incidence $E^i e^{-jk_0 d}$, diffraction E^d, additional term $A_{s,h}$, and reflection $E^r_{s,h}$, are analyzed as follows. From (1), the magnitude of the sum of the diffraction and incidence is the order of $f^{-\frac{1}{2}}$ for $x \to \infty$ as

$$\lim_{x\to\infty} E^d + E^i e^{-jk_0 d} \approx E^i \frac{-e^{-j\frac{\pi}{4}}}{4\sqrt{2\pi k_0}} \cot\frac{\pi - (\phi^d - \phi^i)}{4} \frac{e^{-jk_0 s}}{\sqrt{s}} + E^i e^{-jk_0 d} \sim O\left(k_0^{-\frac{1}{2}}\right) \sim O\left(f^{-\frac{1}{2}}\right) \quad (12)$$

since the modified Fresnel integral $F(\cdot)$ reduces to unit when x is large. It is commonly considered that the diffraction becomes weak with an increase in frequency.

However, in the transition region ($x \to 0$), according to (B3) in Appendix B, the magnitude of the sum of the diffraction and incidence is the order of $f^{\frac{1}{2}}$ as

$$\lim_{x\to 0} E^d + E^i e^{-jk_0 d} \approx \frac{1}{2} E^i e^{-jk_0 d} + E^i \frac{e^{-jk_0 s} e^{j\frac{\pi}{4}}}{\sqrt{2\pi s}} \sqrt{k_0 x} \sim O\left(k_0^{\frac{1}{2}}\right) \sim O\left(f^{\frac{1}{2}}\right) \quad (13)$$

It seems that the opposing frequency characteristic with common sense is obtained in the transition region. The reason is that in the transition region, the sum of the diffraction and incidence is mainly dependent on how much the ratio of the first FZ remains. The size of the first FZ decreases with an increase in frequency. Accordingly, as shown in Fig. 9, the ratio of the first FZ at a high frequency remains more than the case at a low frequency with the same distance x from the edge of the screen to the phase center. Thus, in the transition region, the sum of the diffraction and incidence becomes strong with an increase in frequency.

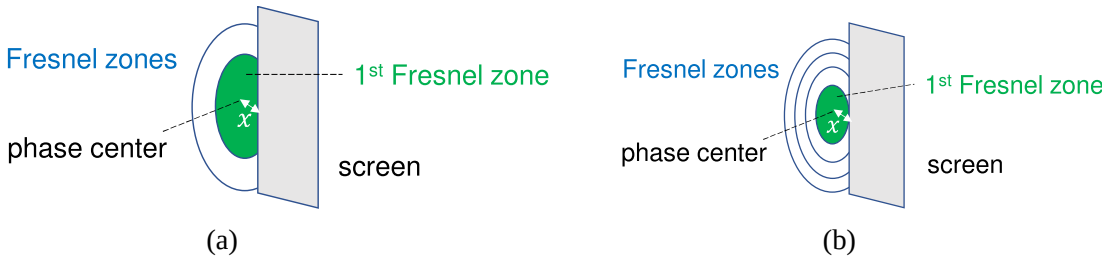

Figure 9. Image of the shadowed FZ in the transition region. (a) Low frequency. (b) High frequency.

On the other hand, from (8) and (10), the magnitude of the additional term is the order of $f^{-\frac{1}{6}}$ as

$$A_{s,h} = -E^i \left(\frac{k_0 a}{2}\right)^{\frac{1}{3}} \sqrt{\frac{2}{k_0}}\, p^*(\xi, q_{s,h}) e^{-j\frac{\xi^3}{12}} e^{-j\frac{\pi}{4}} \frac{e^{-jk_0 s}}{\sqrt{s}} \sim O\left(k_0^{-\frac{1}{6}}\right) \sim O\left(f^{-\frac{1}{6}}\right) \quad (14)$$

It means that the additional term becomes weak with an increase in frequency. In the transition region, the magnitude of the sum of the reflection and incidence is the order of $f^{\frac{1}{2}}$ as

$$\lim_{x\to 0} E^r_{s,h} + E^i e^{-jk_0 d} \approx \lim_{x\to 0} E^d + A_{s,h} + E^i e^{-jk_0 d} \sim O\left(f^{\frac{1}{2}}\right) + O\left(f^{-\frac{1}{6}}\right) \sim O\left(f^{\frac{1}{2}}\right) \quad (15)$$

Therefore, in the transition region, the sum of the reflection and incidence becomes strong with an increase in frequency. Figures 10(a)–(b) show the frequency characteristics among the sum of the diffraction and incidence, the sum of the reflection and incidence, and additional term at the frequencies from 100 to 300 GHz bands when x is set as 0.03 m. The relative complex permittivity of the human skin at the frequency above 100 GHz can be found in [24]. From the results, it can be concluded that the additional term becomes weak while the others become strong in the transition region when frequency increases. In addition, the results show that at a high frequency, the additional term is much weaker than the other terms.

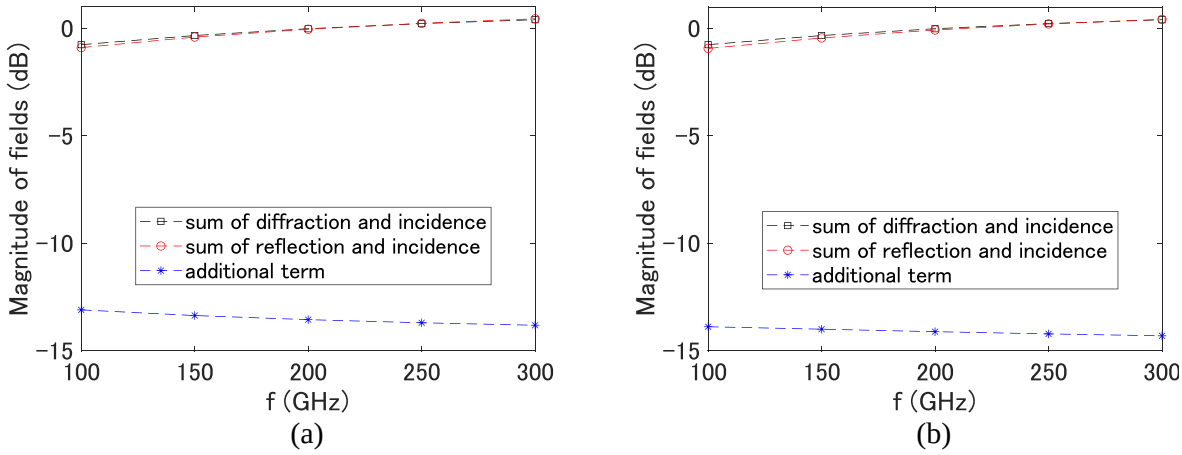

Figure 10. Frequency characteristics among the sum of the diffraction and incidence, the sum of the reflection and incidence, and additional term. (a) Perpendicular polarization. (b) Parallel polarization.

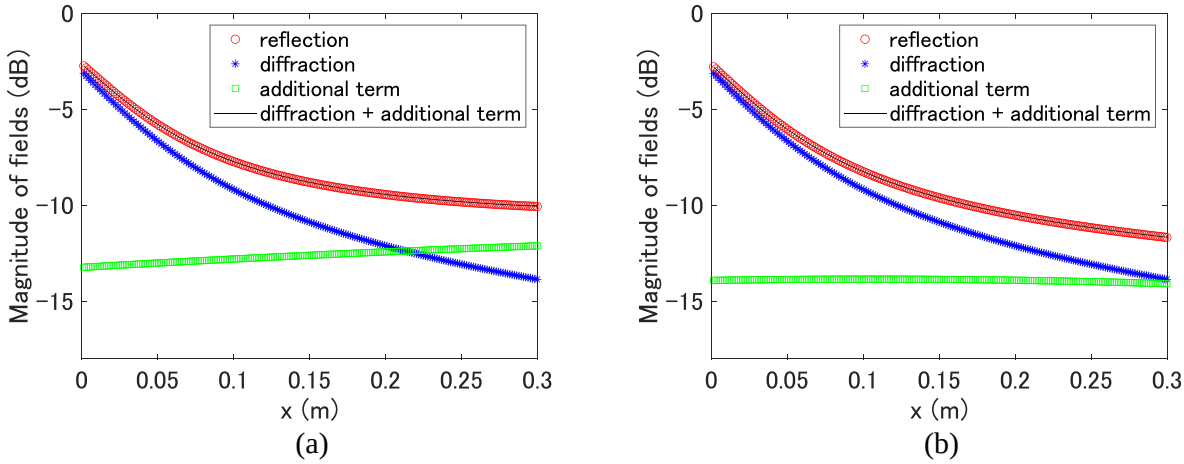

Figure 11. The plots of the magnitude of each field at 100 GHz. (a) Perpendicular polarization. (b) Parallel polarization.

Figures 11–12 show the plots of the magnitude of each field at 100 and 300 GHz, respectively. The results imply that in the transition region ($x \to 0$), the diffraction dominates the reflection in (9) at those high frequencies. Therefore, we find that the contribution of the shadowed FZ is larger than the boundary condition (i.e., the surface impedance and the polarization) to the total field at a high frequency.

The contribution of boundary condition is evaluated by simulating the dependencies of the polarization and material. Figures 13(a)–13(b) show the comparison between the perpendicular polarization and parallel polarization for the human skin at 100 and 300 GHz, respectively. The results imply that there is almost no dependency on polarization. Moreover, Figures 14(a)–14(b) show the comparison between the human skin and perfect electric conductor (PEC) for the perpendicular polarization at 100 and 300 GHz, respectively. The results show that there is almost no dependency on the material. From the above results, we can conclude that the contribution of the shadowed FZ is larger than the boundary condition (i.e., the surface impedance and the polarization) when the opaque object is close to a shadowing boundary in the lit side of the transition region at a high frequency.

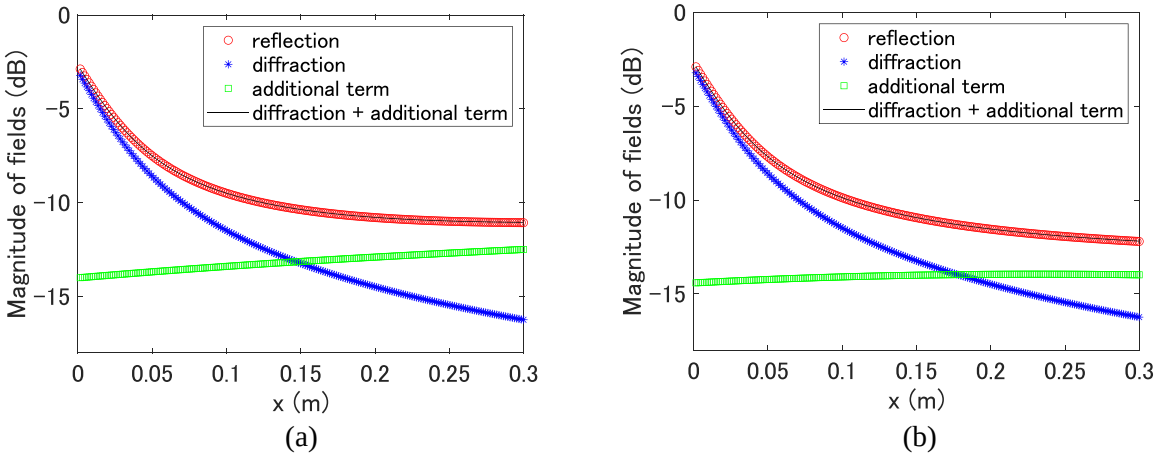

Figure 12. The plots of the magnitude of each field at 300 GHz. (a) Perpendicular polarization. (b) Parallel polarization.

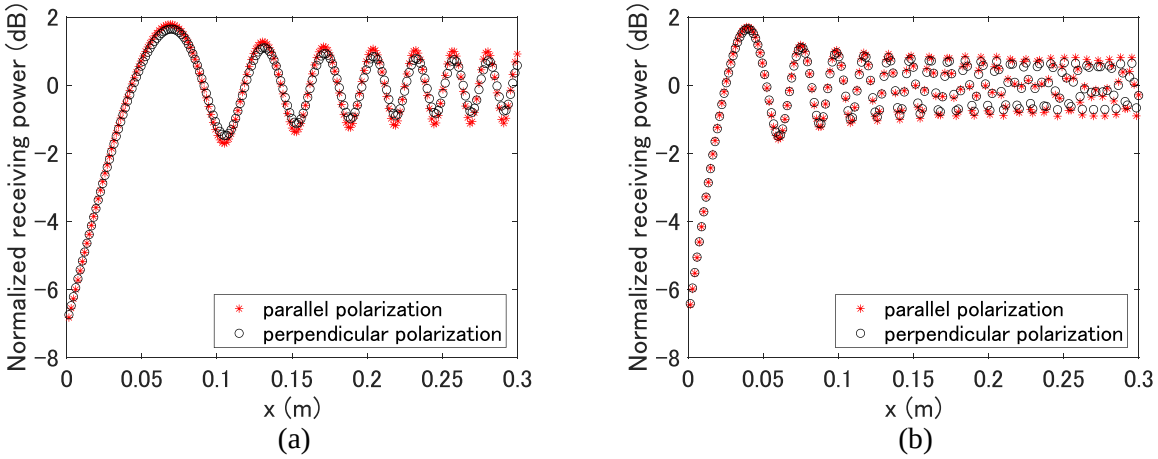

Figure 13. The dependency on polarization. (a) $f = 100$ GHz. (b) $f = 300$ GHz.

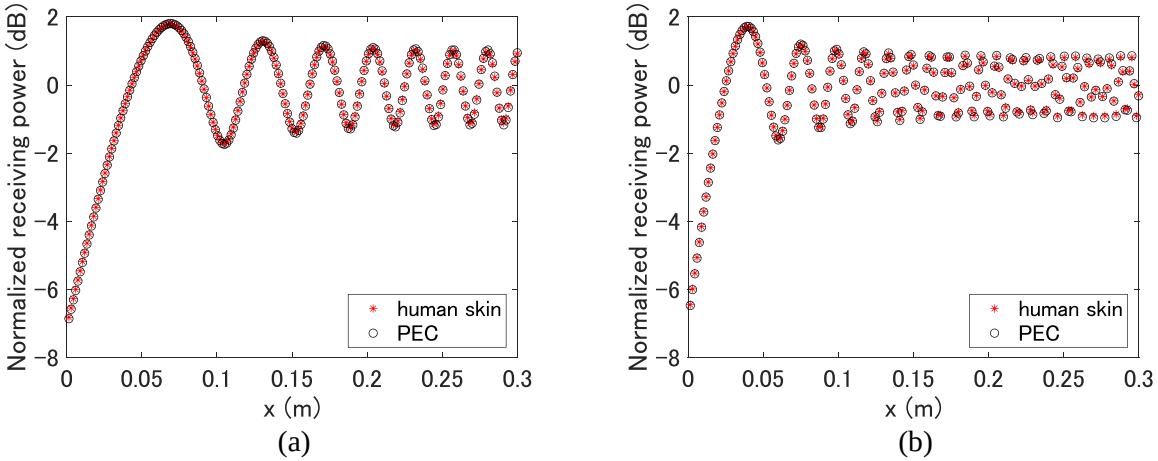

Figure 14. The dependency on the material. (a) $f = 100$ GHz. (b) $f = 300$ GHz.

5. CONCLUSION

This paper derived an additional term based on a UTD to model the difference between the reflection and diffraction from a dielectric circular cylinder and an absorber screen, respectively, in the lit side of the transition region. The proposed model was validated by the UTD and exact solutions of a dielectric circular cylinder at a high frequency. From the proposal, the contributions of the shadowed FZ and boundary conditions (i.e., the surface impedance and the polarization) were separated. The frequency characteristics of the shadowed FZ and boundary conditions were theoretically analyzed. The results showed that the contributions of the boundary conditions are weaker than the shadowed FZ in the lit region at a high frequency. The limitation of this work is that the discussion is only focused on the lit side ($x > 0$) of the transition region. In the future, the derivation of the additional term in the shadowed side ($x < 0$) of the transition region will be analyzed.

ACKNOWLEDGMENT

This paper was supported by the Commissioned Research through the National Institute of Information and Communications Technology (NICT), Japan, under Grant #02701.

APPENDIX A. RELATION BETWEEN THE FRESNEL ZONE NUMBER AND THE DIFFRACTION

A.1. Fresnel Zone Number

We support a transmitter (Tx) and a receiver (Rx) located on the y-axis, and the origin is between the Tx and Rx. The Fresnel zone (FZ) is one of a series of confocal ellipsoidal regions with foci at the Tx and Rx, as shown in Fig. A1. Within the same ellipsoid of the FZ, the phases of all the deflected paths, which are the propagating paths scattered from the boundary of the ellipsoid once time and then radiated to Rx, are the same. Depending on the phase difference between the direct-path and deflected-path waves, the waves can interfere constructively or destructively. The Fresnel zone number n corresponding to the phase difference between the direct path (Tx-Rx path) and the deflected path is defined as

$$\sqrt{d_1^2 + h^2} + \sqrt{d_2^2 + h^2} - (d_1 + d_2) = n\frac{\pi}{2} \tag{A1}$$

where d_1 and d_2 are the distances along the y-axis from the Tx and Rx to the origin, respectively. h is the distance along the x-axis from the boundary of the ellipsoid to the origin.

By using the Fresnel region approximation (FRA) [25], $\sqrt{d_{1,2}^2 + h^2}$ can be approximated as

$$\sqrt{d_{1,2}^2 + h^2} \approx d_{1,2} + \frac{h}{2d_{1,2}} \tag{A2}$$

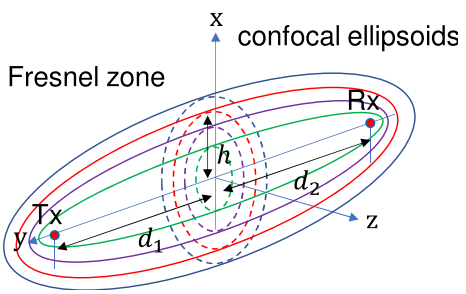

Figure A1. Model of the Fresnel zone.

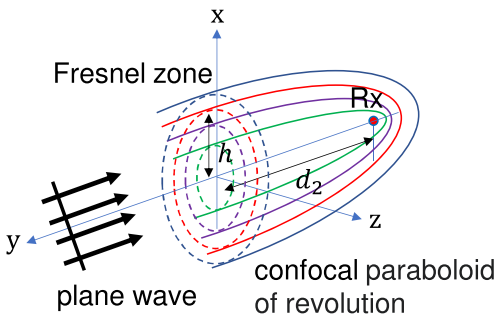

Figure A2. Model of the Fresnel zone for a plane wave incidence.

Accordingly, the Fresnel zone number n can be written as

$$n = \frac{h^2}{\lambda}\left(\frac{1}{d_1} + \frac{1}{d_2}\right) \tag{A3}$$

The direct-path and deflected-path waves interfere destructively when n is an even integer. They interfere constructively when n is an odd integer. That is the meaning of the Fresnel zone number.

In this work, a plane wave incidence is used by assuming that the Tx is placed at infinity. Therefore, the Fresnel zone number is calculated by taking the limiting value as

$$\lim_{d_1\to\infty} n = \frac{\sqrt{d_2^2 + h^2} - h}{\frac{\lambda}{2}} \approx \frac{h^2}{\lambda d_2} \tag{A4}$$

In that case, the FZ is no more the ellipsoid but a parabola of revolution, as shown in Fig. A2.

A.2. Knife-Edge Diffraction Model Based on a Kirchhoff Approximation

We support that $\mathbf{r}'$ and $\mathbf{r}$ are the position vectors of the source and observation point, respectively. A scalar electric field E can be solved by Huygens' principle as

$$E(\mathbf{r}) = E^i(\mathbf{r}) + \oint_{S_1} \left\{G(\mathbf{r},\mathbf{r}')\nabla' E(\mathbf{r}') - \nabla' G(\mathbf{r},\mathbf{r}')E(\mathbf{r}')\right\} \cdot \mathbf{n}' dS' \tag{A5}$$

where $\mathbf{n}'$ is the normal vector of the surface at point of $\mathbf{r}'$. The first term E^i and the second term on the right-hand side of (A5) correspond to the incident and scattered fields, respectively. $G(\cdot)$ is the 3-dimensional (3D) free-space Green function defined as

$$G(\mathbf{r},\mathbf{r}') := \frac{e^{-jk_0|\mathbf{r}-\mathbf{r}'|}}{4\pi|\mathbf{r}-\mathbf{r}'|} \tag{A6}$$

In the Kirchhoff approximation (KA) [7], we do not solve the integral equation but approximate the second source in (A5) as

$$E(\mathbf{r}') \approx \begin{cases} 0 & (\mathbf{r}' \in S_1) \\ E^i(\mathbf{r}') & (\mathbf{r}' \in S_2) \end{cases} \tag{A7}$$

where regions S_1 and S_2 are inside and outside the shadowed region. The KA calculates the field by integrating the second source over the infinite vacuum plane as

$$E(\mathbf{r}) \approx \int_{S_2} \left\{G(\mathbf{r},\mathbf{r}')\nabla' E^i(\mathbf{r}') - \nabla' G(\mathbf{r},\mathbf{r}')E^i(\mathbf{r}')\right\} \cdot (-\mathbf{n}') dS' \tag{A8}$$

with

$$E^i(\mathbf{r}) \approx \int_{S_1+S_2} \left\{G(\mathbf{r},\mathbf{r}')\nabla' E^i(\mathbf{r}') - \nabla' G(\mathbf{r},\mathbf{r}')E^i(\mathbf{r}')\right\} \cdot (-\mathbf{n}') dS' \tag{A9}$$

Figure A3 shows a knife-edge diffraction model (KEDM) [26] for a semi-infinite-height and infinite-long screen. dS' as the infinitesimal second Huygens' source is located on the coordinate of $(x, 0, z)$ in the x-z plane. l_1 and l_2 are the distances from the Tx and Rx to dS', respectively.

The KEDM uses the FRA to approximate $l_{1,2}$ as

$$l_{1,2} \approx \begin{cases} d_{1,2} + \dfrac{x^2+z^2}{2d_{1,2}} & \text{(for phase variations)} \\ d_{1,2} & \text{(for amplitude variations)} \end{cases} \tag{A10}$$

Since $|\mathbf{r}|$ and $|\mathbf{r}'|$ correspond to d_2 and $\sqrt{x^2+z^2}$, respectively, each term in (A8) can be approximated as

$$G(\mathbf{r},\mathbf{r}') \approx \frac{e^{-jk_0\left(d_2 + \frac{x^2+z^2}{2d_2}\right)}}{4\pi d_2} \tag{A11}$$

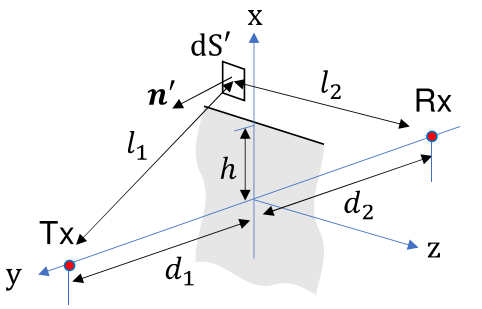

Figure A3. Diffraction by a knife edge.

$$\nabla' E^i(\mathbf{r}') \approx \frac{-jk_0\lambda E_0 e^{-jk_0\left(d_1+\frac{x^2+z^2}{2d_1}\right)}}{4\pi d_1}\frac{\partial l_1}{\partial \mathbf{n}'} \tag{A12}$$

$$\nabla' G(\mathbf{r},\mathbf{r}') \approx \frac{-jk_0 e^{-jk_0\left(d_2+\frac{x^2+z^2}{2d_2}\right)}}{4\pi d_2}\frac{\partial l_2}{\partial \mathbf{n}'} \tag{A13}$$

$$E^i(\mathbf{r}') \approx \frac{\lambda E_0 e^{-jk_0\left(d_1+\frac{x^2+z^2}{2d_1}\right)}}{4\pi d_1} \tag{A14}$$

where E_0 is the electric field of the source. λ is a wavelength. $\mathbf{n}'$ is a normal vector of the screen toward the Tx.

Assuming that Tx/Rx is far away from the screen, the normal derivatives can be approximated as

$$\frac{\partial l_1}{\partial \mathbf{n}'} \approx +1, \quad \frac{\partial l_2}{\partial \mathbf{n}'} \approx -1 \tag{A15}$$

substituting (A11)–(A15) into (A8) as

$$E(\mathbf{r}) \approx \frac{je^{-jk_0(d_1+d_2)}}{4\pi d_1 d_2}\int_h^\infty e^{-jk_0x^2\{1/(2d_1)+1/(2d_2)\}}dx \int_{-\infty}^\infty e^{-jk_0z^2\{1/(2d_1)+1/(2d_2)\}}dz \tag{A16}$$

where h is the distance from the origin to the edge. We let

$$x\sqrt{\frac{2}{\lambda}\left(\frac{1}{d_1}+\frac{1}{d_2}\right)} = X, \quad z\sqrt{\frac{2}{\lambda}\left(\frac{1}{d_1}+\frac{1}{d_2}\right)} = Z \tag{A17}$$

Substituting (A17) into (A16), we have

$$E(\mathbf{r}) \approx \frac{je^{-jk_0(d_1+d_2)}}{4\pi d_1 d_2}\frac{1}{\frac{2}{\lambda}\left(\frac{1}{d_1}+\frac{1}{d_2}\right)}\int_\nu^\infty e^{-j(\pi/2)X^2}dX \int_{-\infty}^\infty e^{-j(\pi/2)Z^2}dZ \tag{A18}$$

We apply the Fresnel integrals $C(\cdot)$ and $S(\cdot)$ as

$$C(\nu) = \int_0^\nu \cos\left(\frac{\pi}{2}\tau^2\right)d\tau \tag{A19}$$

$$S(\nu) = \int_0^\nu \sin\left(\frac{\pi}{2}\tau^2\right)d\tau \tag{A20}$$

$$C(\infty) = S(\infty) = \frac{1}{2} \tag{A21}$$

The integral in (A8) now reads

$$E(\mathbf{r}) \approx j\frac{E^i(\mathbf{r})}{2}(1-j)\left\{0.5 - C(\nu) - j0.5 + jS(\nu)\right\} \tag{A22}$$

where E^i and ν are the incident field in a free space and diffraction parameter, respectively, defined as

$$E^i(\mathbf{r}) = \frac{\lambda E_0 e^{-jk_0(d_1+d_2)}}{4\pi(d_1+d_2)} \tag{A23}$$

$$\nu = h\sqrt{\frac{2}{\lambda}\left(\frac{1}{d_1}+\frac{1}{d_2}\right)} \tag{A24}$$

In the lit region ($\nu < 0$), the total field is considered as the sum of incidence and diffraction as

$$E(\mathbf{r}) = E^i(\mathbf{r}) + E^d(\mathbf{r}) \tag{A25}$$

In the shadowed region ($\nu > 0$), the total field is considered as diffraction alone as

$$E(\mathbf{r}) = E^d(\mathbf{r}) \tag{A26}$$

From (A22), (A25), and (A26), we can conclude that the diffraction normalized by an incidence $|E^d(\mathbf{r})/E^i(\mathbf{r})|$ is directly associated with the diffraction parameter ν. According to (A3) and (A24), we can link the relationship between the diffraction parameter and Fresnel zone number as

$$n = \frac{\nu^2}{2} \tag{A27}$$

Therefore, the diffraction loss of a knife edge is determined by the shadowed FZ alone.

APPENDIX B. DERIVATION OF THE ADDITIONAL TERM

As shown in Fig. B1(a), when x is small, the small argument of the diffraction coefficient derived in [10] is approximated as

$$D \approx \frac{-\sqrt{2\pi k_0 s^d} + 2k_0 s^d\left(\pi - (\phi^d - \phi^i)\right)e^{j\frac{\pi}{4}}}{2\sqrt{2\pi k_0}} \tag{B1}$$

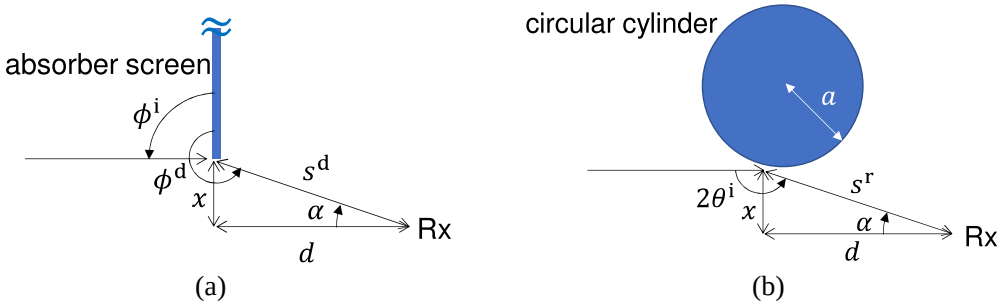

Figure B1. Parameters of the UTD. (a) Model of an absorber screen. (b) Model of a dielectric circular cylinder.

Since the diffraction and reflection points can be seen as one point for $x \to 0$, $\phi^d - \phi^i$ can be approximated as $2\theta^i$, as shown in Fig. B1(b). In addition, for $x \to 0$, $2\theta^i$ can be considered as the supplementary angle of α. By applying the small argument of the sine function, we have

$$\pi - \left(\phi^d - \phi^i\right) \approx \pi - 2\theta^i = \alpha \approx \sin\alpha \approx \frac{x}{s^d} \tag{B2}$$

Substituting (B1) and (B2) into (1), we can asymptotically approximate the diffracted field as

$$E^d \approx -\frac{1}{2}E^i e^{-jk_0 s^d} + E^i \frac{e^{-jk_0 s^d} e^{j\frac{\pi}{4}}}{\sqrt{2\pi s^d}}\sqrt{k_0}x \tag{B3}$$

On the other hand, (5) and the square root factor in (3) can be approximated as

$$\xi = -2M\cos\left(\frac{\pi}{2}-\frac{\alpha}{2}\right) = -2M\sin\frac{\alpha}{2} \approx -M\alpha \approx -M\frac{x}{s^r} \tag{B4}$$

$$\sqrt{\frac{a\cos\theta^i}{a\cos\theta^i + 2s^r}} \approx \sqrt{\frac{1}{2s^r}} \tag{B5}$$

where the vertical component of s^r is also considered as x because of $s^d \approx s^r$ for $x \to 0$. The associated Fock-type integral in (B6) and the small argument of the Fresnel integral in (B7) are applied as

$$\hat{P}(\xi, q_{s,h}) = \left(p^*(\xi, q_{s,h}) - \frac{1}{2\sqrt{\pi}\xi}\right) e^{-j\frac{\pi}{4}} \tag{B6}$$

$$F(X) \approx \left(\sqrt{\pi X} - 2Xe^{j\frac{\pi}{4}}\right) e^{j\left(\frac{\pi}{4}+X\right)} \tag{B7}$$

Substituting (B4)–(B7) into (3), we can asymptotically approximate the reflected field as

$$E^r_{s,h} \approx -\frac{1}{2}E^i e^{-jk_0 s^r} + E^i \frac{e^{-jk_0 s^r} e^{j\frac{\pi}{4}}}{\sqrt{2\pi s^r}} \sqrt{k_0 x} + A_{s,h} \tag{B8}$$

$$A_{s,h} := -E^i M \sqrt{\frac{2}{k_0}} p^*(\xi, q_{s,h}) e^{-j\frac{\xi^3}{12}} e^{-j\frac{\pi}{4}} \frac{e^{-jk_0 s}}{\sqrt{s}} \tag{B9}$$

Therefore, by comparing (B3) and (B8), the authors propose the additional term $A_{s,h}$ as the difference between the reflection from a dielectric circular cylinder and the diffraction from an edge.

APPENDIX C. EXACT SOLUTION OF A DIELECTRIC CIRCULAR CYLINDER

C.1. Perpendicular Polarization

As shown in Fig. C1(a), we assume that the electric field of a uniform plane wave polarized in the z direction is incident along the x-axis. The incident electric field at the coordinate of (ρ, ϕ) can be expressed as

$$\mathbf{E}^i = \hat{\mathbf{z}} E^i_z = \hat{\mathbf{z}} E_0 e^{-jk_0 \rho \cos\phi} \tag{C1}$$

where $\hat{\mathbf{x}}$, $\hat{\mathbf{y}}$, and $\hat{\mathbf{z}}$ are the unit vectors of the x, y, and z directions, respectively. ρ and ϕ are the parameters of the cylindrical coordinate system. The z subscript of E is directly associated with the z component of the electric field. E_0 is the magnitude of the electric field of the source.

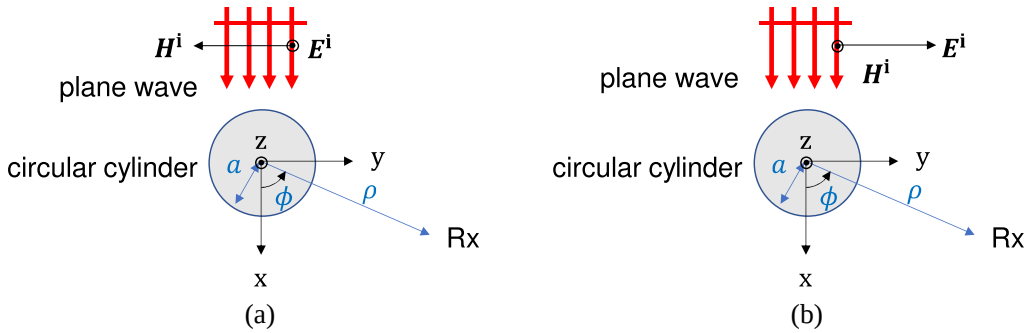

Figure C1. Parameters of the exact solution of a dielectric circular cylinder. (a) Perpendicular polarization. (b) Parallel polarization.

The scattered electric field $\mathbf{E}^s$ derived from [17] can be written as

$$\mathbf{E}^s = \hat{\mathbf{z}} E_0 \sum_{n=-\infty}^{\infty} j^{-n} \frac{-\sqrt{\frac{\epsilon_r}{\mu_r}} J_n(k_0 a) J'_n(k_d a) + J'_n(k_0 a) J_n(k_d a)}{\sqrt{\frac{\epsilon_r}{\mu_r}} H^{(2)}_n(k_0 a) J'_n(k_d a) - H^{(2)'}_n(k_0 a) J_n(k_d a)} H^{(2)}_n(k_0 \rho) e^{jn\phi} \tag{C2}$$

where a, ϵ_r, and μ_r are the radius, relative complex permittivity, and relative permeability of the circular cylinder, respectively. k_d is the wave number in the dielectric cylinder. The functions $J_n(\cdot)$ and $H_n^{(2)}(\cdot)$ are the Bessel function of the first kind and the Hankel function of the second kind, respectively, for the n^{th} order.

C.2. Parallel Polarization

As shown in Fig. C1(b), we assume that the electric field of a uniform plane wave polarized in the y direction is incident along the x-axis. The incident magnetic field at the coordinate of (ρ, ϕ) can be expressed as

$$\mathbf{H}^i = \hat{\mathbf{z}} H_z^i = \hat{\mathbf{z}} H_0 e^{-jk_0\rho\cos\phi} \tag{C3}$$

where the z subscript of H is directly associated with the z component of the magnetic field. H_0 is the magnitude of the magnetic field of the source.

The scattered magnetic field $\mathbf{H}^s$ derived from [17] can be written as

$$\mathbf{H}^s = \hat{\mathbf{z}} H_0 \sum_{n=-\infty}^{\infty} j^{-n} \frac{-\sqrt{\frac{\mu_r}{\epsilon_r}} J_n(k_0a) J_n'(k_da) + J_n'(k_0a) J_n(k_da)}{\sqrt{\frac{\mu_r}{\epsilon_r}} H_n^{(2)}(k_0a) J_n'(k_da) - H_n^{(2)'}(k_0a) J_n(k_da)} H_n^{(2)}(k_0\rho) e^{jn\phi} \tag{C4}$$

REFERENCES

1. Andrews, J. G., S. Buzzi, W. Choi, S. V. Hanly, A. Lozano, A. C. K. Soong, and J. C. Zhang, "What will 5G be?" *IEEE J. Sel. Areas Commun.*, Vol. 32, No. 6, 1065–1082, Jun. 2014.
2. Rangan, S., T. S. Rappaport, and E. Erkip, "Millimeter-wave cellular wireless networks: Potentials and challenges," *Proc. IEEE*, Vol. 102, No. 3, 366–385, Mar. 2014.
3. Rappaport, T. S., Y. Xing, O. Kanhere, S. Ju, A. Madanayake, S. Mandal, A. Alkhateeb, and G. C. Trichopoulos, "Wireless communications and applications above 100 GHz: Opportunities and challenges for 6G and beyond," *IEEE Access*, Vol. 7, 78729–78757, 2019.
4. MacCartney, G. R., S. Deng, S. Sun, and T. S. Rappaport, "Millimeter-wave human blockage at 73 GHz with a simple double knife-edge diffraction model and extension for directional antennas," *2016 IEEE 84th Vehi. Tech. Conf. (VTC-Fall)*, 1–6, Montreal, QC, Canada, 2016.
5. Sun, S., T. S. Rappaport, R. W. Heath, A. Nix, and S. Rangan, "MIMO for millimeter-wave wireless communications: Beamforming, spatial multiplexing, or both?," *IEEE Commun. Mag.*, Vol. 52, No. 12, 110–121, Dec. 2014.
6. Sun, S., G. R. MacCartney, M. K. Samimi, and T. S. Rappaport, "Synthesizing omnidirectional antenna patterns, received power and path loss from directional antennas for 5G millimeter-wave communications," *Proc. IEEE Global Commun. Conf. (GLOBECOM)*, 3948–3953, San Diego, CA, USA, Dec. 2015.
7. Du, X., K. Saito, J.-I. Takada, and P. Hanpinitsak, "A novel mirror Kirchhoff approximation method for predicting the shadowing effect by a metal cuboid," *Progress In Electromagnetics Research M*, Vol. 104, 199–212, 2021.
8. Du, X. and J. Takada, "Mirror Kirchhoff approximation for predicting shadowing effect by a PEC convex cylinder," *2021 Appl. Computa. Electromagn. Soci.*, Hamilton, Canada, Aug. 2021.
9. Du, X. and J. Takada, "Low computational cost mirror Kirchhoff approximation for predicting shadowing effect," *IEEE Access*, Vol. 10, 23829–23841, 2022.
10. Kouyoumjian, R. G. and P. H. Pathak, "A uniform geometrical theory of diffraction for an edge in a perfectly conducting surface," *Proc. IEEE*, Vol. 62, No. 11, 1448–1461, Nov. 1974.
11. Andersen, J. B., "UTD multiple-edge transition zone diffraction," *IEEE Trans. Antennas Propag.*, Vol. 45, No. 7, 1093–1097, Jul. 1997.

12. Pathak, P. H., W. Burnside, and R. Marhefka, "A uniform GTD analysis of the diffraction of electromagnetic waves by a smooth convex surface," *IEEE Trans. Antennas Propag.*, Vol. 26, No. 5, 631–642, Sep. 1980.
13. Pathak, P. H., "An asymptotic analysis of the scattering of plane waves by a smooth convex cylinder," *Radio Science*, Vol. 14, No. 3, 419–435, Jun. 1979.
14. Pearson, L., "A scheme for automatic computation of Fock-type integrals," *IEEE Trans. Antennas Propag.*, Vol. 35, No. 10, 1111–1118, Oct. 1987.
15. Qi, Y., B. Currie, W. Wang, P. Y. Chung, C. Wu, and J. Litva, "Measurement and simulation of radio wave propagation in two indoor environments," *Proc. 6th Inter. Symp. Pers.*, 1171–1174, Toronto, Ontario, Canada, 1995.
16. Jacob, M., S. Priebe, A. Maltsev, A. Lomayev, V. Erceg, and T. Kürner, "A ray tracing based stochastic human blockage model for the IEEE 802.11ad 60 GHz channel model," *Proc. 5th Euro. Conf. Antennas Propag. (EUCAP)*, 3084–3088, Rome, Italy, 2011.
17. Balanis, C. A., *Advanced Engineering Electromagnetics*, Wiley, Hoboken, New Jersey, USA, 1989.
18. Villanese, F., N. E. Evans, and W. G. Scanlon, "Pedestrian-induced fading for indoor channels at 2.45, 5.7 and 62 GHz," *2000 IEEE 52th Vehi. Tech. Conf. (VTC-Fall)*, 43–48, Boston, MA, USA, 2000.
19. Fakharzadeh, M., J. Ahmadi-Shokouh, B. Biglarbegian, M. R. Nezhad-Ahmadi, and S. Safavi-Naeini, "The effect of human body on indoor radio wave propagation at 57–64 GHz," *2009 IEEE Antennas Propag. Soc. Inter. Symp.*, 1–4, North Charleston, SC, USA, 2009.
20. Duarte Carvalho de Queiroz, A. and L. C. Trintinália, "An analysis of human body shadowing models for ray-tracing radio channel characterization," *2015 SBMO/IEEE MTT-S Inter. Microwave Optoelectron. Conf. (IMOC)*, 1–5, Porto de Galinhas, Brazil, 2015.
21. Tang, C., "Back scattering from dielectric-coated infinite cylindrical obstacles," *J. Appl. Phys.*, Vol. 28, No. 5, 628–633, 1957.
22. Jacob, M., S. Priebe, T. Kürner, M. Peter, M. Wisotzki, R. Felbecker, and W. Keusgen, "Fundamental analyses of 60 GHz human blockage," *Proc. 7th Euro. Conf. Antennas Propag. (EuCAP)*, 117–121, Gothenburg, Sweden, 2013.
23. Wu, T., T. S. Rappaport, and C. M. Collins, "The human body and millimeter-wave wireless communication systems: Interactions and implications," *2015 IEEE Inter. Conf. Communi. (ICC)*, London, UK, 2015.
24. Gandhi, O. P. and A. Riazi, "Absorption of millimeter waves by human beings and its biological implications," *IEEE Trans. Microw. Theory Tech.*, Vol. 34, No. 2, 228–235, Feb. 1986.
25. Southwell, W. H., "Validity of the Fresnel approximation in the near field," *J. Opt. Soc.*, Vol. 71, No. 1, 7–14, 1981.
26. Haykin, S. and M. Moher, *Modern Wireless Communications*, 24–29, Library of Congress Cateloging-in-Publication, 2003.